Chemical Engineering Journal 493 (2024) 152539

Contents lists available at ScienceDirect

Chemical Engineering Journal

journal homepage: www.elsevier.com/locate/cej

Pyridine substitution strategy for one-dimensional perovskite: Toward efficient and stable mixed-dimensional photovoltaics

Xianfang Zhou [a,b], Xiao Liang [a,b], Fei Wang [a,b], Huajun Sun [a,*], Quanyao Zhu [a,*], Hanlin Hu [b,*]

[a] State Key Laboratory of Advanced Technology for Materials Synthesis and Processing, School of Materials Science and Engineering, Wuhan University of Technology, Wuhan, China
[b] Hoffmann Institute of Advanced Materials, Postdoctoral Innovation Practice Base, Shenzhen Polytechnic, Nanshan District, Shenzhen, China

ARTICLE INFO

Keywords:
1D/3D perovskite
Ionic liquid
Perovskite Solar Cell
Long-term Stability
Surface passivation

ABSTRACT

Surface passivation *via* one-dimensional (1D) perovskite has emerged as a promising method to suppress trap states and enhance charge extraction and transportation, leading to improved efficiency and long-term stability. Ionic liquid engineering, characterized as environmental-green additive, has shown particular promise in this regard. Herein, we explore the influence of the electronegativity and dipole moment of two different ionic liquids, benzamidine hydrochloride (BZ) and 2-amidinopyridine hydrochloride (2AP), on the formation of 1D perovskite and the performance of resulting devices. An effective passivation 1D layer has been formed through post-treatment, resulting in nano-rod crystal modified morphology with effectively passivated defects at grain boundaries, enhanced hydrophobicity, prolonged charge carrier lifetime, tailored energy level, and decreased trap density. Notably, the perovskite film treated with 2AP exhibited superior performance due to its stronger interaction with 3D perovskite and better passivation ability on defects originating from the presence of a pyridine ring. As a result, the PSCs incorporating 2AP achieved a champion power conversion efficiency of 24.55 % and retain 90 % of their initial efficiency after storage for over 1000 h at room temperature under ~ 50 % RH conditions without encapsulation. This study provides valuable insights for expanding the selection of ionic liquids applied in 1D perovskite-assisted surface passivation towards efficient and stable photovoltaics.

1. Introduction

Perovskite solar cells (PSCs) have attracted significant attention due to their impressive merits in the photovoltaic field, such as their high absorption coefficient [1], tunable bandgap [2], and high mobility of charge carriers [3], all of which endow themselves with enormous potential in achieving high power conversion efficiency (PCE). Over the past decades, numerous researchers have devoted considerable efforts to raising the PCE from 3.8 % to 26.1 % [4], which is approaching that of mature commercial silicon-based solar cells [5]. However, the solution-processing method will inevitably lead to the formation of unfavorable defects distributed at the surface and grain boundaries (GBs) [6–10]. These defects not only serve as the centers of harmful non-radiative recombination and the initial points of destructive decomposition triggered by external shocks such as high temperature, strong light exposure, and moisture invasion but also inhibit the charge transfer between the perovskite and adjacent transport layers [11–17]. This results in the critically weakened photovoltaic performance of the device. Therefore, it is essential to seek effective ways to passivate the perovskite surface defects.

The surface modification of one-dimensional (1D) perovskites has been considered a promising strategy to simultaneously suppress defects and enhance long-term stability [18–20]. Compared with traditional three-dimensional (3D) perovskites, 1D perovskites exhibit stronger hydrophobicity, due to their large-size organic spacer cations, which effectively prevent moisture penetration, thus improving stability. Furthermore, two-dimensional (2D) perovskites which share similar characteristics with 1D perovskites, tend to grow parallel to the substrate. This orientation results in unsatisfactory out-of-plane charge transport ability and limited photovoltaic performance. In contrast, 1D perovskites demonstrate relatively superior charge transport characteristics and offer more flexible structural configurations [18,21,22]. Moreover, specific functional groups in 1D perovskites may also contribute to defect passivation. However, the intrinsic photovoltaic characteristics of 1D perovskites are significantly worse than those of 3D perovskites. This is primarily attributed to the poor charge conductivity

* Corresponding authors.
E-mail addresses: huajunsun@whut.edu.cn (H. Sun), cglamri@whut.edu.cn (Q. Zhu), hanlinhu@szpu.edu.cn (H. Hu).

https://doi.org/10.1016/j.cej.2024.152539
Received 25 March 2024; Received in revised form 12 May 2024; Accepted 24 May 2024
Available online 24 May 2024

caused by the steric hindrance effect of the large spacer cations [18]. To address this issue, researchers have widely adopted small organic conjugated spacers in surface modification to construct mixed-dimensional structure which can promote efficiency without sacrificed charge transfer ability. Gao *et, al.* [23] modified 3D perovskite by depositing thiazole ammonium (TA) through a gas-pump drying-assisted two-step process. More important, the introduction of the 1D capping layer effectively passivated 3D perovskite films, leading to enhanced charge transport, prolonged carrier lifetime, and prevention of iodide ion migration. Wang *et al.* [24] employed 4-chlorobenzamidine hydrochloride (CBAH) as spacer to form orientational 1D nanorod-like 1D perovskite on the surface of $FAPbI_3$ perovskite, which simultaneously regulated the crystallization and promoted charge extraction, the corresponding PSC exhibited a raised PCE of 21.95 %. Li and co-workers [25] introduced 1,10-phenanthroline (Phen) to form 1D perovskite passivation layer on the surface of 3D perovskite film, the device based on 1D/3D stacked configuration exhibit a best efficiency of 23.3 %. Cha *et al.* [26] fabricated a lattice-matched 1D/3D hybrid perovskite structure with pyridinium bromide (PyBr), a rising PCE of 23.74 % was achieved by corresponding PSC. Despite the progress in surface modification of 1D perovskite, it is still critical to expand the choices of appropriate ligands for further improvement of efficiency and stability which are extraordinary essential for widespread application in the future.

In this study, we introduced two structurally similar conjugated spacer molecules, benzamidine hydrochloride (BZ) and 2-amidinopyridine hydrochloride (2AP), which contain a benzene ring and a pyridine ring, respectively, onto the surface of a 3D perovskite film to form a 1D perovskite passivation layer. We systematically investigated the performance differences resulting from the structural diversity of these two ionic liquids. Chemical characterization and theoretical calculations revealed that 2AP exhibits a relatively stronger interaction with PbI_2 and 3D perovskites due to the pyridine substitution strategy, leading to more effective suppression of defects. The presence of the 1D perovskite passivation layer on the surface of the 3D perovskite film significantly improved film quality, resulting in a smoother surface and reduced trap-density. Additionally, energy level tailoring achieved through the incorporation of the 1D perovskite facilitated charge transfer and extraction. Consequently, we achieved champion efficiencies of 23.17 % and 24.55 % for devices treated with BZ and 2AP, respectively. Furthermore, due to the prominent hydrophobicity of passivation layer, unencapsulated devices retained 86.3 % (BZ) and 90.7 % (2AP) of initial PCE after 1000 h aging in ambient condition under ~ 50 % RH.

2. Results and discussion

The chemical structure and calculated electrostatic potential (ESP) distribution maps are shown in Fig. 1(a). Both BZ and 2AP possess the same ammonium branch chains but different hexatomic rings (benzene and pyridine). Specifically, one carbon atom in the benzene ring has been replaced by a nitrogen atom, which has a higher electronegativity. This substitution directly alters the ESP distribution and dipole moment of original molecule. The presence of heteroatom (nitrogen atom) in 2AP allows the pyridine ring to act as a much stronger negative charge center (yellow and red) compared to the benzene ring in BZ. This property makes 2AP more effective in passivating Lewis-acid defects, such as uncoordinated Pb^{2+} according to the Lewis acid-base effect [27,28]. Additionally, the larger dipole moment of 2AP (2.99 Debye) than that of BZ (2.82 Debye) implies the stronger interaction between $[PbI_6]^{4-}$ octahedron and 2AP [29,30]. Therefore, a simple substitution in molecular configuration might result in significant changes in chemical properties.

To investigate the differences in chemical properties between BZ and 2AP resulting from their molecular configuration, we conducted liquid-state hydrogen nuclear magnetic resonance (^{1}H NMR) spectroscopy. Samples for liquid-state NMR analysis were prepared by dissolving pure ionic liquid or ionic liquid with PbI_2 in a 1:1 mass ratio in Dimethyl

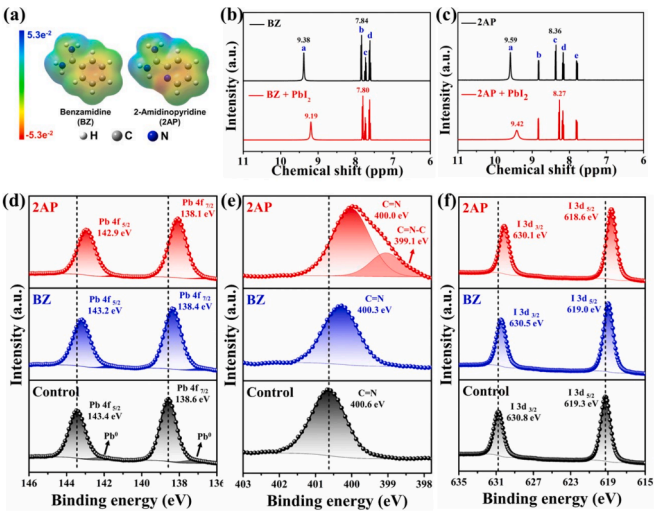

Fig. 1. (a) Chemical structures and electrostatic potential (ESP) distribution maps of BZ and 2AP. (b and c) 1H NMR spectra of pure ionic liquid and ionic liquid mixed with PbI_2 solutions. XPS spectra of Pb 4f (d), C 1 s (e) and I 3d (f) for the control and treated perovskite films.

sulfoxide-d6 (DMSO-d_6) solvent. The results were shown in Fig. 1b, c. The proton signal of $-NH^{2+}$ in BZ and 2AP shifted from 9.38 ppm and 9.59 ppm to 9.19 ppm and 9.42 ppm, respectively, confirming the existence of strong hydrogen bonding between ammonium groups in both ionic liquids and PbI_2 [31]. More importantly, the proton signal of –CH– in the hexatomic rings showed notably different distributions, stemming from the substitution of benzene ring by pyridine ring. The larger chemical shift of 2AP (0.09 ppm) than that of BZ (0.04 ppm) indicates a much stronger interaction between hexatomic rings and PbI_2.

The impacts of nitrogen substitution on interaction between ionic liquids and perovskite were further elucidated through X-ray photoelectron spectroscopy (XPS). Control and ionic liquid treated perovskite films were fabricated and characterized, with the survey spectra and binding energies of diverse elements were shown in Fig. 1(d-f) and Fig. S1. It is evident that the characteristic peaks of Pb $4f_{5/2}$ and Pb $4f_{7/2}$, located at 143.4 eV and 138.6 eV in control sample, shifted to lower binding energies by 0.2 eV and 0.5 eV for BZ- and 2AP- treated samples, respectively. These shifts, attributed to the increase in electron cloud density, indicate that 2AP can form a much more effective coordination with Pb^{2+}. Notably, the control sample exhibited two bulges at 142.1 eV and 137.2 eV, corresponding to metallic Pb_0, which ultimately led to the formation of undesired defects in the perovskite film. As the Pb^{2+} is the right state for lead element in perovskite, the remarkably decrease in the content of Pb^0 shown in Fig. S2 indicates the modification of BZ and 2AP effectively suppressed the defects in perovskite films. Fig. 1(e) shows the N 1 s spectra, where a new peak at 399.1 eV appeared in 2AP sample, attributed to pyridine N (C = N-C) [32,33], confirming the existence of 2AP in modified perovskite film. Moreover, the characteristic peak of N 1 s in FA^+ gradually shifted to lower binding energy, revealing the electron-rich environment of FA^+ possibly caused by the electron-donating effect of benzene and pyridine rings. Similarly, offsets to lower binding energies were observed in I 3d spectra in Fig. 1(f), indicating enhanced electrostatic interaction of hydrogen or ionic bonding after the introducing of BZ and 2AP. Consequently, both BZ and 2AP could not only coordinated with uncoordinated Pb^{2+} and formed strong interactions between ionic liquids and perovskite *via* hydrogen or ionic bonding but also inhibited the formation of defect-states, such as Pb^0. Significantly, 2AP exhibited stronger coordination interaction with perovskite material and more effective suppression of defect states formation compared to BZ.

Based on the benefits of interaction between two ionic liquids and perovskite and suppression of defect formation, we introduced BZ and

2AP onto the surface of 3D perovskite film and successfully fabricated high quality mixed-dimensional perovskite films. Fig. 2(a) illustrates the post-treatment procedure of surface modification, with the concentration optimized to 2 mg/mL for surface treatment, unless stated otherwise. The surface morphology images of modified perovskite films were obtained by scanning electron microscopy (SEM) as shown in Fig. 2(b) and Fig. S3. The image of control sample shows a typical morphology of polycrystalline perovskites, with distinct GBs which tend to induce non-radiative recombination of charge carriers can be obviously observed [34]. The post-thermal annealing treated perovskite films exhibited extraordinarily different morphologies, with numerous rod-shaped crystals homogeneously distributed on the whole surface of samples, and the GBs became difficult to distinguish, similar appearances also occur in lower or higher concentration samples. Moreover, the water resistance of control and treated films was verified by water contact angles measurements, with the insets of Fig. 2(b) showing the corresponding water contact angle images. The measured values of treated films were 65.7° and 69.6° for BZ and 2AP, respectively, both of which were larger than that of control film (55.1°). The larger contact angle, attributed to the existence of hydrophobic 1D perovskite, demonstrates enhanced moisture resistance and improved long-term stability achieved through surface modification [21]. These results indicate the formation of 1D perovskite at GBs, thus optimizing the surface defects of 3D perovskite and improved stability, eventually obtaining high quality perovskite films with improved device performance.

To delve deeper into the impacts of incorporated 1D perovskite on surface morphology and electrical properties, we performed atomic force microscopy (AFM) and Kelvin probe force microscopy (K-PFM) to obtain height maps (Fig. 2c) and contact potential maps (Fig. 2d) of control and treated films. All height maps match well with SEM images. According to the root-mean-square (RMS) roughness measurement and height amplitude curves (Fig. S4), modified films exhibit lower RMS roughness values than control film, with the 2AP-treated film having the smoothest surface. Regarding electrical properties, inhomogeneous dark or bright areas distributed all over the contact potential maps of the control and BZ-treated films. However, the 2AP-treated film exhibited a much more uniform distribution. The potential amplitude curves in Fig. S5 reveal that the surface potential of the control, 2AP- treated, and BZ-treated films increase sequentially, corresponding to the decreases in work function, which can facilitate the charge transfer and extraction [35,36].

To further investigate the interaction between ionic liquids and PbI_2, as well as the mechanism of defect passivation by the modification of BZ and 2AP, we conducted density functional theory (DFT) calculations to analyze and compare these two ionic liquids from a theoretical perspective. Fig. 3(a, b) illustrates the charge density difference of PbI_2 decorated by BZ and 2AP, with charge accumulation and depletion represented by yellow and red color, the molecular modeling structure of PbI_2 was shown in Fig. S6. The results were displayed in Fig. 3(c), the adsorption energy and binding energy between BZ and PbI_2 were calculated to be −0.90 and −0.95 eV, respectively. For 2AP, these values are −0.98 and −1.05 eV, the lower adsorption energy and binding energy suggesting a distinctly stronger coordination between 2AP and PbI_2, which is favorable for the formation of 1D perovskite. Furthermore, this conclusion is consistent with the enhanced interactions between 2AP and PbI_2 or 3D perovskite compared with BZ, as discussed earlier. Additionally, it aligns with the observed improvement in hydrophobicity, as reflected in the larger water contact angle. More importantly, Fig. 3(d,e) display the optimized surface structure and charge density difference of 3D perovskite modified with BZ and 2AP. The modification of BZ and 2AP significantly altered the formation energy of the iodine vacancy (V_I), considered one of the most major defects

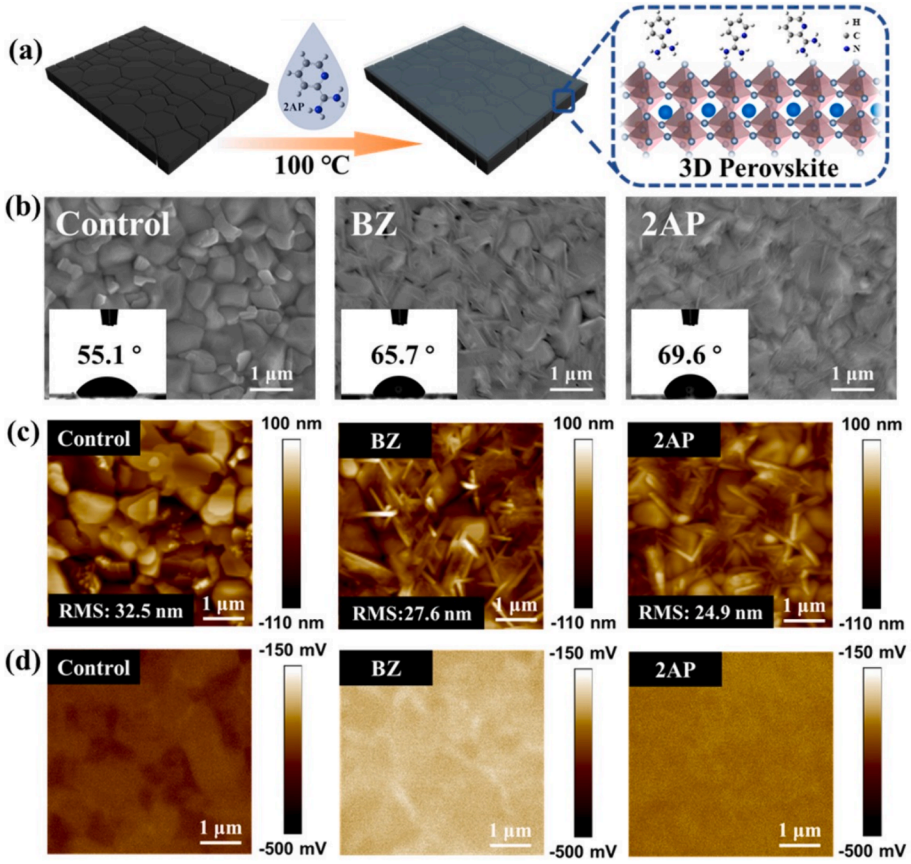

Fig. 2. (a) Schematic diagram of the post-treatment procedure of the surface modification. (b) Top-view SEM images of the control, BZ-treated and 2AP-treated perovskite films (insets: the corresponding water contact angles). AFM (c) and K-PFM (d) images of the control, BZ-treated and 2AP-treated perovskite films.

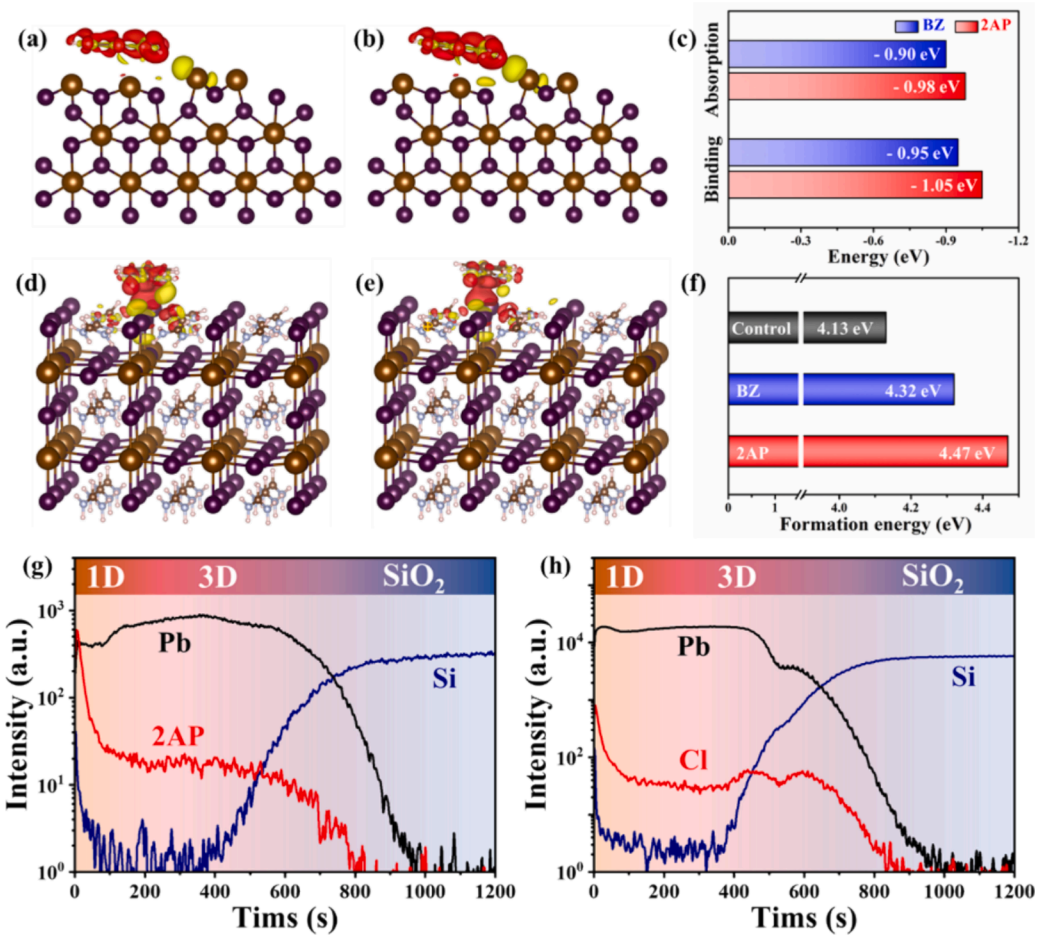

Fig. 3. The charge density difference of PbI_2 decorated by BZ (a) and 2AP (b) with charge accumulation and depletion represented by yellow and red color. (c) The absorption energy and binding energy of BZ and 2AP. The charge density difference of 3D perovskite modified with BZ (d) and 2AP (e) with charge accumulation and depletion represented by yellow and red color. (f) The formation energy of VI in control and treated perovskite films. The TOF-SIMS depth profiles of cations (g) and anions (h). (For interpretation of the references to color in this figure legend, the reader is referred to the web version of this article.)

in the perovskite system we studied [37–39]. Specifically, the formation energy of V_I increased from 4.13 eV of control film to 4.32 and 4.47 eV for BZ- and 2AP- treated films, respectively (Fig. 3f). The higher formation energy of V_I indicates the effective passivation of surface defects has been achieved through the post-treating with BZ and 2AP. This is beneficial for preventing performance degradation caused by surface defects with chemical reactivity, even after the crystallization process of the 3D perovskite has been completed. To investigate ion diffusion, we conducted the time-of-flight secondary-ion mass spectrometry (TOF-SIMS) to confirm the distribution of ionic liquids in the 2AP-treated perovskite film, as shown in Fig. 3(g,h). The signals of both $2AP^+$ and Cl^- exhibited a similar distribution trend, mainly concentrated on the surface with slight presence throughout the 3D perovskite layer. This suggests that the effective passivation of surface defects has been achieved through post-processing modification. In addition, the mass spectra of 2AP-treated perovskite film were presented in Fig. S7, with prominent peaks at the mass-to-charge ratio (m/z) of 122 and 35 corresponded to the signal of $2AP^+$ and Cl^-, respectively.

Grazing-incidence wide-angle X-ray scattering (GIWAXS) measurement were conducted to investigate the effect of surface modification on the crystallinity of perovskite, the incident angle was selected to be 0.5°, which was more instrumental for exploring the near-surface region. The GIWAXS patterns of the control, BZ- and 2AP- treated perovskite films are displayed in Fig. 4(a-c), the diffraction rings at 0.9 and 1 $Å^{-1}$ in control sample correspond to the remnant PbI_2 phase and (1 1 0) plane of 3D perovskite, respectively. With post-treatment, new scattering ring occurs at 0.55 $Å^{-1}$ in BZ- treated sample, corresponding to the formation of 1D $BZPbI_3$ [19,40]. Meanwhile, new scattering rings at 0.5, 0.6 and 9.5 $Å^{-1}$ can be observed in 2AP- treated sample, indicating the exact existence of new substance on 3D perovskite. The radically integrated intensity curves of all samples have been summarized in Fig. S8, which are consistent with X-ray diffraction (XRD) patterns (Fig. S9). To further identify the new substance on the surface of 3D perovskite, we deposited 2AP on PbI_2 layer and conducted GIWAXS characterizations of fabricated film, as shown in Fig. S10. The integrated curves were displayed in Fig. S11, and the SEM image were presented in Fig. S12. Additionally, we have prepared the $2APPbI_3$ single crystal (Fig. S13), which exhibits a consistent XRD pattern with the aforementioned film (Fig. S14). Subsequently, we employed single crystal X-ray diffraction (SCXRD) to confirm the precise structure of $2APPbI_3$ as shown in Fig. S15, ensuring the 1D chain configuration of $2APPbI_3$. Moreover, the signal intensity of PbI_2 slightly decreased after post-processing, suggesting that excess PbI_2 has been consumed during the formation of 1D $2APPbI_3$.

Ultraviolet – visible (UV – vis) absorption spectra and ultraviolet photoelectron spectroscopy (UPS) spectra were adopted to illustrate the effect of surface treatment on the energy alignment of perovskite. The treated films exhibit almost unchanged UV–vis absorption spectra (Fig. S16), demonstrating the slightly incorporation of 1D perovskite did not affect the essential light-absorption ability of the 3D perovskite film. Therefore, the band gap measured from Tauc-plots (Fig. S17) remains a constant value of 1.57 eV. The valence band maximum (VBM) was obtained by combing the cutoff edge and work function that calculated

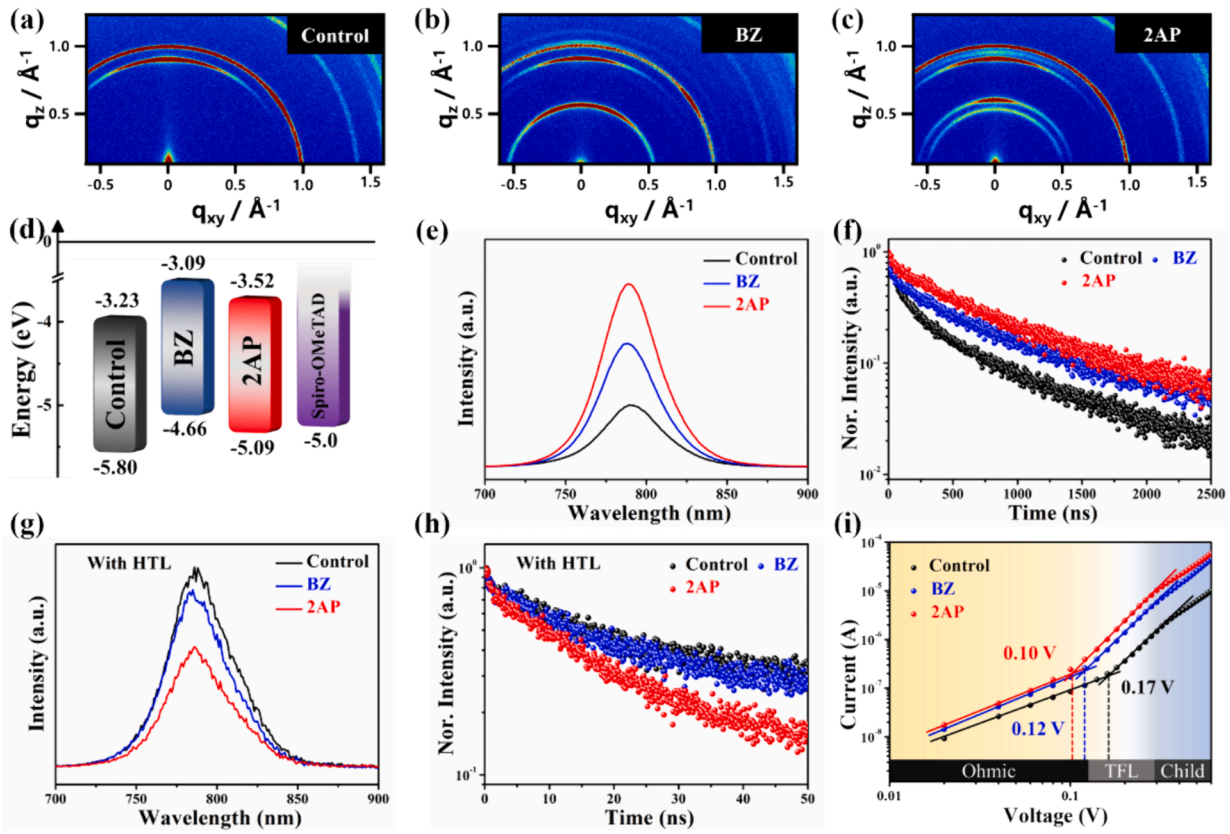

Fig. 4. GIWAXS images of the control (a), BZ- treated (b) and 2AP- treated (c) perovskite films. (d) Energy level diagram of the control and treated perovskite films. (e) PL spectra and (f) TRPL spectra of the perovskite films without and with surface treatment. (g) PL spectra and (h) TRPL spectra of perovskite films with the hole transport layer. (i) Dark I-V curves of the hole-only SCLC devices.

from Fermi edge. Subsequently, the conduct band minimum (CBM) was calculated according to the obtained optical band gap and VBM (Fig. S18), eventually yielding the specific energy level of the perovskite film, as shown in Fig. 4(d). The calculated CBM increased from −5.80 to −4.66 and −5.09 eV for BZ- and 2AP- treated sample, respectively. Meanwhile, VBM changed from −3.23 to −3.09 and −3.52 eV, respectively. Such a gradient arrangement of the energy level could effectively promote the transportation and extraction of charge-carriers, which is favorable to improvement of device performance of PSCs [35,41].

To examine the effect of incorporated 1D perovskite on the photoelectric properties of perovskite films, we employed steady-state photoluminescence (PL) and time-resolved photoluminescence (TRPL) to investigate the charge-carrier dynamics in control and treated films. Both BZ- and 2AP- treated films exhibit remarkably improved PL intensities (Fig. 4e), with the 2AP-treated film showing more pronounced improvement, implying a significant improvement in film quality with less trap states. It is noteworthy that the emission peak of the BZ- and 2AP- treated films show a blue shift compared to the control film, indicating the effective passivation effect of the formed 1D perovskite on the surface of 3D perovskite film [42–44]. The results of TRPL measurements shown in Fig. 4(f) further confirmed this conclusion. The TRPL decay curves were fitted a biexponential function and the fitting parameters were summarized in Table S1. The calculated average lifetime (τ_{ave}) of the control perovskite film was 464 ns, which was significantly increased to 613 and 744 ns for BZ- and 2AP- treated film, respectively. The enhanced PL intensity and prolonged TRPL lifetime validly suggest that the incorporation of 1D perovskite effectively diminished non-radiative recombination by passivating surface defects. At the same time, such modification did not damage the intrinsic properties of 3D perovskite. Moreover, we have also conducted PL and TRPL measurements to control and treated samples with an additional hole transport layer deposited on the surface, as shown in Fig. 4(g, h). The treated samples exhibit reduced PL intensity and shortened TRPL lifetime compared to the control sample, indicating facilitated carrier extraction between functional layer and hole transport layer. It is worth noting that 2AP-treated sample exhibited better performance than BZ-treated sample, which might be attributed to better contact owing to smoother surface measured from AFM and more appropriate energy level alignment as mentioned above.

We then employed the space-charge-limited current (SCLC) method to estimate the trap-state densities of control and modified perovskite films. The tested devices were constructed with the following layers: glass/ITO/PEDOT: PSS/Perovskite/Spiro-OMeTAD/Au. Fig. 4(i) shows the dark current–voltage (*I-V*) curves of fabricated hole-only devices. From each curve, we obtained the trap-filled limit voltage (V_{TFL}) value, and further estimate the trap density (N_t) using the equation $N_t = (2\varepsilon_r\varepsilon_0 V_{TFL})/(qL)^2$, where ε_r and ε_0 are the relative dielectric constant of perovskite and vacuum permittivity, respectively, q is the element charge and L is the thickness of the perovskite layer [21,45,46]. It is apparent to observe V_{TFL} of control film decreased from 0.17 V to 0.12 V and 0.10 V for BZ- and 2AP- treated films, respectively. Consequently, the corresponding calculated N_t also reduced from 2.29×10^{15} cm^{-3} to 1.62×10^{15} cm^{-3} and 1.35×10^{15} cm^{-3}, demonstrating the efficient defect passivation has been achieved through the incorporation of 1D perovskite.

To evaluate the impact of surface modification of 1D perovskite on the photovoltaic performance of PSCs, planar n-i-p devices with structure of glass/ITO/SnO_2/perovskite/Spiro-OMeTAD/Au were fabricated and characterized. Fig. 5(a) displays a cross-sectional SEM image of 2AP-treated device, the cross-view images of control and BZ-treated devices were shown in Fig. S19. Notably, the absence of GBs in the vertical direction allowed perovskite crystals to directly contact

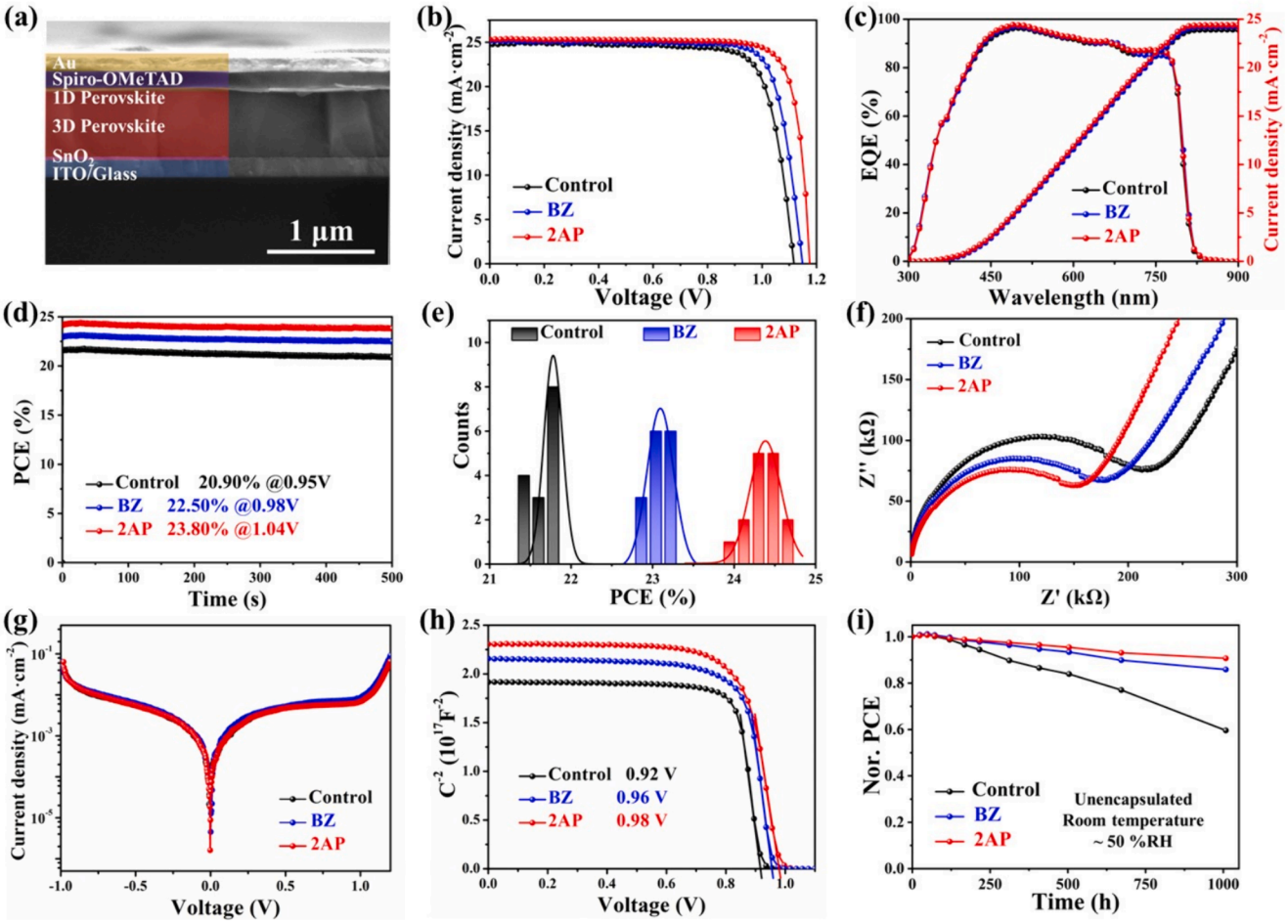

Fig. 5. (a) Cross-view SEM image of the 2AP-treated PSC. The *J-V* curves (b), EQE curves and the corresponding integrated current densities (c) and the stabilized output efficiency (d) of the champion devices based on control and treated perovskite films. (e) Histogram of PCE based on 15 individual devices. (f) Nyquist plots, (g) dark $J-V$ curves and (h) Mott − Schottky plots of the PSCs based on control and treated perovskite films. (i) Normalized PCE decline of unencapsulated control and treated devices at room temperature under ~ 50 % RH condition.

adjacent charge transport layers, which was beneficial for carrier transportation and collection. The *J-V* curves of the champion control and treated devices under standard AM 1.5 G illumination are displayed in Fig. 5(b), the corresponding photovoltaic parameters are presented in Table S2. The control device exhibited an efficiency of 21.76 % with V_{oc} of 1.116 V, J_{sc} of 24.91 mA•cm^{-2} and FF of 78.3 %, meanwhile the BZ-treated device delivered a higher PCE of 23.17 % with a V_{oc} of 1.148 V, a J_{sc} of 25.14 mA•cm^{-2} and FF of 80.3 %. However, 2AP- treated device achieved the best PCE of 24.55 % with the V_{oc} of 1.169 V, J_{sc} of 25.33 mA•cm^{-2} and FF of 82.9 %. The optimal concentration of 2AP was obtained by comparing PL spectra with different concentrations and the *J-V* curves of corresponding PSCs as shown in Figs. S20 and S21. Fig. 5 (c) shows the External quantum efficiency (EQE) spectra and the corresponding integrated current densities of champion devices, the integrated Jsc were calculated to be 23.93, 24.25 and 24.39 mA•cm^{-2} for the control, BZ- and 2AP- treated devices, respectively, which match well with J_{sc} in *J-V* curves. It is worth noting that we have summarized the PCE of reported 1D/3D mixed-dimensional PSCs including our research as shown in Table S3. The stabilized maximum power point (MPP) tracking was conducted to evaluate the continuous output performance of devices, as shown in Fig. 5(d). The BZ- and 2AP- treated devices stabilized at efficiency of 22.50 % and 23.80 % for 500 s, respectively; however, the control device just delivered an efficiency of 20.90 %. We have fabricated and measured 15 individual devices of each sample and display the PCE histogram and statistical distributions in Fig. 5(e) and Fig. S22. The results demonstrate reliable reproducibility and significant improvement in photovoltaic performance based on 1D perovskite surface modification strategy.

To further investigate the charge behaviors in control and treated devices, electrochemical impedance spectroscopy (EIS) measurement was conducted to study the interfacial charge transport and recombination of PSCs. The Nyquist plots are shown in Fig. 5(f). It can be clearly observed that each curve is divided into two semi- arcs, which relate to the charge transport resistance (R_{ct}) in low frequency area and the recombination resistance (R_{rec}) in high frequency area [47,48]. Compared to the control device, both treated devices exhibit decreased R_{ct} and increased R_{rec}. Notably, 2AP- treated device deliver the lowest R_{ct} and the highest R_{rec}, indicating the promoted charge transfer ability and distinctly suppressed non-radiation recombination. Fig. 5(g) shows the dark *J-V* curves of control and treated devices. The lower dark current densities of treated device suggest the decrease of leakage current which is mainly ascribed to the non-radiation recombination caused by defects, indicating the effective passivation of defect which is consistent with the above results [49,50]. The Mott-Schottky curves were measured to analyze the built-in potential (V_{bi}) of PSCs (Fig. 5h). The value of V_{bi} increased from 0.92 V to 0.96 V and 0.98 V with BZ-and 2AP-treated, respectively. The improvement of V_{bi} is conducive to the separation of photogenerated carriers and suppression of non-radiation recombination of carriers [32,41]. Generally, the above results illustrated that the remarkable PV performance improvement of treated devices was attributed to facilitated charge carrier transport and separation, reduced trap-states density, and inhibited non-radiation

recombination.

In addition to efficiency, long-term stability is another critical factor for evaluating the quality of PSCs. As mentioned earlier, the incorporation of 1D perovskite leads to enhanced hydrophobicity, we have aged and characterized unencapsulated PSCs at room temperature under ~ 50 % RH condition to study their stability performance. The efficiencies of unencapsulated devices that stored in ambient conditions were tracked for six weeks, as shown in Fig. 5(i). The BZ- and 2AP- treated devices maintained 86.3 % and 90.7 % of initial efficiencies after about 1000 h, respectively, whereas the control device only remained less than 60 % of its original efficiency. Moreover, we conducted in-situ UV–vis absorption measurement to investigate the effect of ILs modification on the thermal stability of perovskite films, as shown in Fig. S23. Under continuous heating at 150 ℃ and ~ 30 % RH condition, the control film began to decay in the initial stage, while the BZ- and 2AP-treated films exhibited a decline phenomenon after approximately 20 and 35 min, respectively. Additionally, we tracked the efficiency decline of unencapsulated PSCs at 85 ℃ under ~ 50 % RH condition (Fig. S24). The BZ- and 2AP- treated PSCs retained 61.4 % and 70.2 % of their initial efficiencies after about 100 h, respectively, compared to less than 30 % for the control PSC device.

3. Conclusion

In summary, we have successfully incorporated two ionic liquids (BZ and 2AP) in 3D perovskite, leading to significant surface optimization through the formation of a 1D perovskite passivation layer. Substitution the benzene ring with a pyridine ring notably enhanced the interaction between ionic liquids and PbI_2 or 3D perovskite, resulting in superior film quality characterized by optimized morphology, enhanced hydrophobicity, prolonged charge carrier lifetime, tailored energy level and reduced trap density upon 2AP incorporation. Ultimately, we fabricated optimized devices based on 2AP treatment, achieving a champion PCE of 24.55 %, along with notably improved long-term stability. This work provides valuable insights for expanding ionic liquids selection in 1D perovskite assisted surface modification strategy to realize efficient and stable PSCs for further commercialization.

CRediT authorship contribution statement

Xianfang Zhou: Writing – original draft, Visualization, Project administration, Methodology, Investigation, Data curation. **Xiao Liang:** Writing – review & editing, Project administration, Methodology, Investigation. **Fei Wang:** Writing – review & editing, Project administration, Methodology, Investigation. **Huajun Sun:** Writing – review & editing. **Quanyao Zhu:** Writing – review & editing. **Hanlin Hu:** Writing – review & editing, Supervision, Project administration, Funding acquisition, Data curation.

Declaration of competing interest

The authors declare that they have no known competing financial interests or personal relationships that could have appeared to influence the work reported in this paper.

Data availability

The authors do not have permission to share data.

Acknowledgments

This work is supported by the Scientific Research Startup Fund for Shenzhen High-Caliber Personnel of Shenzhen Polytechnic No. 6022310038k. The financial support from Guangdong Basic and Applied Basic Research Foundation (No. 2023A1515011677), Shenzhen Science and Technology Innovation Commission (Project No. JCYJ20200109105003940; Project No. 20220811205532001) is gratefully acknowledged.

Appendix A. Supplementary data

Supplementary data to this article can be found online at https://doi.org/10.1016/j.cej.2024.152539.

References

[1] G. Xing, N. Mathews, S. Sun, S.S. Lim, Y.M. Lam, M. Grätzel, S. Mhaisalkar, T. C. Sum, Long-range balanced electron- and hole-transport lengths in organic-inorganic $CH_3NH_3PbI_3$, Science 342 (2013) 344–347, https://doi.org/10.1126/science.1243167.

[2] T. Jesper Jacobsson, J.-P. Correa-Baena, M. Pazoki, M. Saliba, K. Schenk, M. Grätzel, A. Hagfeldt, Exploration of the compositional space for mixed lead halogen perovskites for high efficiency solar cells, Energy Environ Sci 9 (2016) 1706–1724, https://doi.org/10.1039/C6EE00030D.

[3] J.J. Yoo, G. Seo, M.R. Chua, T.G. Park, Y. Lu, F. Rotermund, Y.-K. Kim, C.S. Moon, N.J. Jeon, J.-P. Correa-Baena, V. Bulović, S.S. Shin, M.G. Bawendi, J. Seo, Efficient perovskite solar cells via improved carrier management, Nature 590 (2021) 587–593, https://doi.org/10.1038/s41586-021-03285-w.

[4] A. Kojima, K. Teshima, Y. Shirai, T. Miyasaka, Organometal halide perovskites as visible-light sensitizers for photovoltaic cells, J Am Chem Soc 131 (2009) 6050–6051, https://doi.org/10.1021/ja809598r.

[5] H. Min, D.Y. Lee, J. Kim, G. Kim, K.S. Lee, J. Kim, M.J. Paik, Y.K. Kim, K.S. Kim, M. G. Kim, T.J. Shin, S., Il Seok, Perovskite solar cells with atomically coherent interlayers on SnO_2 electrodes, Nature 598 (2021) 444–450, https://doi.org/10.1038/s41586-021-03964-8.

[6] B. Chen, P.N. Rudd, S. Yang, Y. Yuan, J. Huang, Imperfections and their passivation in halide perovskite solar cells, Chem Soc Rev 48 (2019) 3842–3867, https://doi.org/10.1039/C8CS00853A.

[7] J. Chen, N.-G. Park, Materials and methods for interface engineering toward stable and efficient perovskite solar cells, ACS Energy Lett 5 (2020) 2742–2786, https://doi.org/10.1021/acsenergylett.0c01240.

[8] W. Zhang, T. Zhang, L. Qin, S.-Z. Kang, Y. Zhao, X. Li, Anti-solvent engineering to rapid purify PbI_2 for efficient perovskite solar cells, Chem. Eng. J. 479 (2024) 147838, https://doi.org/10.1016/j.cej.2023.147838.

[9] Q. Wang, X. Jiang, C. Peng, J. Zhang, H. Jiang, H. Bu, G. Yang, H. Wang, Z. Zhou, X. Guo, Regulating the lattice strain in perovskite films to obtain efficient and stable perovskite solar cells, Chem. Eng. J. 481 (2024) 148464, https://doi.org/10.1016/j.cej.2023.148464.

[10] Y. Lei, Y. Xu, M. Wang, G. Zhu, Z. Jin, Origin, influence, and countermeasures of defects in perovskite solar cells, Small 17 (2021) 2005495, https://doi.org/10.1002/smll.202005495.

[11] M.L. Agiorgousis, Y.-Y. Sun, H. Zeng, S. Zhang, Strong covalency-induced recombination centers in perovskite solar cell material $CH_3NH_3PbI_3$, J Am Chem Soc 136 (2014) 14570–14575, https://doi.org/10.1021/ja5079305.

[12] W. Li, Y.-Y. Sun, L. Li, Z. Zhou, J. Tang, O.V. Prezhdo, Control of charge recombination in perovskites by oxidation state of halide vacancy, J Am Chem Soc 140 (2018) 15753–15763, https://doi.org/10.1021/jacs.8b08448.

[13] S.-H. Turren-Cruz, A. Hagfeldt, M. Saliba, Methylammonium-free, high-performance, and stable perovskite solar cells on a planar architecture, Science 362 (2018) 449–453, https://doi.org/10.1126/science.aat3583.

[14] J. Wang, W. Li, W. Yin, Passivating Detrimental DX Centers in $CH_3NH_3PbI_3$ for Reducing Nonradiative Recombination and Elongating Carrier Lifetime, Adv. Mater. 32 (2020) 1906115, https://doi.org/10.1002/adma.201906115.

[15] Z. Zhang, J. Liu, H. Bi, L. Wang, Q. Shen, S. Hayase, Over 14% efficiency of highly reproducible Sn perovskite solar cell via defect passivation and morphology repairment, Chem. Eng. J. 483 (2024) 149345, https://doi.org/10.1016/j.cej.2024.149345.

[16] Z. Xie, S. Chen, Y. Pei, L. Li, S. Zhang, P. Wu, Enhanced efficiency in two-terminal all-perovskite tandem solar cells via binary functional high polymer doping strategy, Chem. Eng. J. 482 (2024) 148638, https://doi.org/10.1016/j.cej.2024.148638.

[17] J. Heo, S.W. Lee, J. Yong, H. Park, Y.K. Lee, J. Shin, D.R. Whang, D.W. Chang, H. J. Park, Interfacial modification of wide-bandgap perovskite solar cell approaching 20% with organic hole transport material, Chem. Eng. J. 474 (2023) 145632, https://doi.org/10.1016/j.cej.2023.145632.

[18] Y. Zhan, F. Yang, W. Chen, H. Chen, Y. Shen, Y. Li, Y. Li, Elastic lattice and excess charge carrier manipulation in 1D–3D perovskite solar cells for exceptionally long-term operational stability, Adv. Mater. 33 (2021), https://doi.org/10.1002/adma.202105170.

[19] J. Wu, H. Zeng, Y. Li, Z. Jiang, C. Liu, J. Zhang, X. Zhou, B. Hu, J. Chen, H. Hu, D. Wang, Y. Zhang, Y. Liu, Z. Liu, X. Wang, B. Xu, Tailoring two-dimensional ruddlesden-popper perovskite via 1D perovskitoid enables efficient and stable solar cells, ACS Energy Lett 8 (2023) 637–646, https://doi.org/10.1021/acsenergylett.2c02373.

[20] P. Liu, Y. Xian, W. Yuan, Y. Long, K. Liu, N.U. Rahman, W. Li, J. Fan, Lattice-matching structurally-stable 1D@3D perovskites toward highly efficient and stable solar cells, Adv Energy Mater 10 (2020) 1903654, https://doi.org/10.1002/aenm.201903654.

[21] F. Wang, D. Duan, K. Zhou, Y.Z.B. Xue, X. Liang, X. Zhou, C. Ge, C. Zhou, J. Xiang, J. Zhu, Q. Zhu, H. Lin, Y. Shi, Y. Chen, G. Li, H. Hu, Ionic liquid engineering enabled in-plane orientated 1D perovskite nanorods for efficient mixed-dimensional perovskite photovoltaics, InfoMat 5 (2023) e12459.
[22] F. Wang, K. Zhou, C. Zhou, X. Liang, T. Wang, Y. Sun, Y. Li, Q. Li, X. Zhou, G. Yang, D. Duan, J. Zhu, Q. Zhu, H. Lin, Y. Shi, C. Yang, G. Xing, H. Hu, Ionic liquid-induced 1D perovskite: exploring 1D perovskite structure to 1D/3D heterojunction-based photovoltaics, Adv Energy Mater 2400021 (2024) 1–11, https://doi.org/10.1002/aenm.202400021.
[23] L. Gao, I. Spanopoulos, W. Ke, S. Huang, I. Hadar, L. Chen, X. Li, G. Yang, M. G. Kanatzidis, Improved environmental stability and solar cell efficiency of (MA, FA)Pb_I3 perovskite using a wide-band-gap 1D thiazolium lead iodide capping layer strategy, ACS Energy Lett 4 (2019) 1763–1769, https://doi.org/10.1021/acsenergylett.9b00930.
[24] J. Wang, L. Liu, S. Chen, L. Qi, M. Zhao, C. Zhao, J. Tang, X. Cai, F. Lu, T. Jiu, Growth of 1D nanorod perovskite for surface passivation in $FAPbI_3$ perovskite solar cells, Small 18 (2022) 1–9, https://doi.org/10.1002/smll.202104100.
[25] Q. Chen, K. Deng, Y. Shen, L. Li, Stable one dimensional (1D)/three dimensional (3D) perovskite solar cell with an efficiency exceeding 23%, InfoMat 4 (2022) 1–9, https://doi.org/10.1002/inf2.12303.
[26] J. Cha, C. Beom Lee, S. Min Park, D. Baek, S. Kim, S. Gyo Han, H. Jin, S. Joo Yang, J. Lim, K. Kim, M. Kim, Lattice-matched in-situ-formed 1D perovskite phase in Multi-dimensional solar cells achieving high phase stability and favorable energy landscape, Chemical Engineering Journal 484 (2024) 149280, https://doi.org/10.1016/j.cej.2024.149280.
[27] H. Zhu, S. Wu, J. Yao, R. Chen, M. Pan, W. Chen, J. Zhou, W. Zhang, T. Wang, W. Chen, An effective surface modification strategy with high reproducibility for simultaneously improving efficiency and stability of inverted MA-free perovskite solar cells, J Mater Chem A Mater 7 (2019) 21476–21487, https://doi.org/10.1039/C9TA07238A.
[28] S. Yu, J. Meng, Q. Pan, Q. Zhao, T. Pullerits, Y. Yang, K. Zheng, Z. Liang, Imidazole additives in 2D halide perovskites: impacts of –CN *versus* $–CH_3$ substituents reveal the mediation of crystal growth by phase buffering, Energy, Environ Sci 15 (2022) 3321–3330, https://doi.org/10.1039/D2EE00571A.
[29] Y. Zheng, X. Wu, R. Zhuang, C. Tian, A. Sun, C. Tang, Y. Liu, Y. Hua, C.C. Chen, Managing interfacial hot-carrier cooling and extraction kinetics for inverted ma-free perovskite solar cells over 23% efficiency via dion-jacobson 2D capping layer, Adv Funct Mater 33 (2023) 2300576, https://doi.org/10.1002/adfm.202300576.
[30] R. Shi, Z. Zhang, W.-H. Fang, R. Long, Charge localization control of electron–hole recombination in multilayer two-dimensional Dion-Jacobson hybrid perovskites, J Mater Chem A Mater 8 (2020) 9168–9176, https://doi.org/10.1039/D0TA01944E.
[31] J. Wang, H. Ma, A. Wang, Z. Li, J. Dong, Y. Liu, S. Gao, S. Yan, X. Chen, Y. Li, Z. Wu, W. Xu, F. Liu, F. Wang, W. Huang, T. Qin, An ammonium-pseudohalide ion pair for synergistic passivating surfaces in $FAPbI_3$ perovskite solar cells, Matter 5 (2022) 2209–2224, https://doi.org/10.1016/j.matt.2022.04.006.
[32] Y. Wu, Q. Wang, Y. Chen, W. Qiu, Q. Peng, Stable perovskite solar cells with 25.17% efficiency enabled by improving crystallization and passivating defects synergistically, Energy, Environ Sci 15 (2022) 4700–4709, https://doi.org/10.1039/D2EE02277J.
[33] Q. Cao, Y. Li, Y. Zhang, J. Zhao, T. Wang, B. Yang, X. Pu, J. Yang, H. Chen, X. Chen, X. Li, S. Ghasemi, H. Salari, A. Hagfeldt, X. Li, N-type conductive small molecule assisted 23.5% efficient inverted perovskite solar cells, Adv Energy Mater 12 (2022) 2201435, https://doi.org/10.1002/aenm.202201435.
[34] Z. Liu, F. Cao, M. Wang, M. Wang, L. Li, Observing defect passivation of the grain boundary with 2-aminoterephthalic acid for efficient and stable perovskite solar cells, Angew. Chem. Int. Ed. 59 (2020) 4161–4167, https://doi.org/10.1002/anie.201915422.
[35] L. Liu, J. Tang, S. Li, Z. Yu, J. Du, L. Bai, X. Li, M. Yuan, T. Jiu, Multi-site intermolecular interaction for in situ formation of vertically orientated 2D passivation layer in highly efficient perovskite solar cells, Adv Funct Mater (2023), https://doi.org/10.1002/adfm.202303038.
[36] R. Chen, H. Shen, Q. Chang, Z. Tang, S. Nie, B. Chen, T. Ping, B. Wu, J. Yin, J. Li, N. Zheng, Conformal imidazolium 1D perovskite capping layer stabilized 3D perovskite films for efficient solar modules, Adv. Sci. 9 (2022) 2204017, https://doi.org/10.1002/advs.202204017.
[37] T. Yang, L. Gao, J. Lu, C. Ma, Y. Du, P. Wang, Z. Ding, S. Wang, P. Xu, D. Liu, H. Li, X. Chang, J. Fang, W. Tian, Y. Yang, S. Liu, K. Zhao, One-stone-for-two-birds strategy to attain beyond 25% perovskite solar cells, Nat Commun 14 (2023) 839, https://doi.org/10.1038/s41467-023-36229-1.
[38] X. Liang, K. Zhou, D. Duan, F. Wang, C. Ge, X. Zhou, M. Yuan, Y. Shi, H. Lin, Q. Zhu, G. Li, H. Hu, Metal-organic framework nanocrystals enabled efficient and durable two-step perovskite photovoltaics, Chem. Eng. J. 459 (2023) 141524, https://doi.org/10.1016/j.cej.2023.141524.
[39] R. Wang, J. Xue, K.-L. Wang, Z.-K. Wang, Y. Luo, D. Fenning, G. Xu, S. Nuryyeva, T. Huang, Y. Zhao, J.L. Yang, J. Zhu, M. Wang, S. Tan, I. Yavuz, K.N. Houk, Y. Yang, Constructive molecular configurations for surface-defect passivation of perovskite photovoltaics, Science 366 (2019) 1509–1513, https://doi.org/10.1126/science.aay9698.
[40] F. Wang, T. Wang, Y. Sun, X. Liang, G. Yang, Q. Li, Y. Li, X. Zhou, Q. Zhu, A. Ng, H. Lin, M. Yuan, Y. Shi, T. Wu, H. Hu, Two-step perovskite solar cells with $>$ 25% efficiency: unveiling the hidden bottom surface of perovskite layer, Adv. Mater. (2024), https://doi.org/10.1002/adma.202401476.
[41] G. Li, J. Song, J. Wu, Z. Song, X. Wang, W. Sun, L. Fan, J. Lin, M. Huang, Z. Lan, P. Gao, Efficient and stable 2D@3D/2D perovskite solar cells based on dual optimization of grain boundary and interface, ACS Energy Lett 6 (2021) 3614–3623, https://doi.org/10.1021/acsenergylett.1c01649.
[42] A.F. Xu, N. Liu, F. Xie, T. Song, Y. Ma, P. Zhang, Y. Bai, Y. Li, Q. Chen, G. Xu, Promoting thermodynamic and kinetic stabilities of FA-based perovskite by an in situ bilayer structure, Nano Lett 20 (2020) 3864–3871, https://doi.org/10.1021/acs.nanolett.0c00988.
[43] X. Li, W. Zhang, X. Guo, C. Lu, J. Wei, J. Fang, Constructing heterojunctions by surface sulfidation for efficient inverted perovskite solar cells, Science 375 (2022) 434–437, https://doi.org/10.1126/science.abl5676.
[44] T. Kong, H. Xie, Y. Zhang, J. Song, Y. Li, E.L. Lim, A. Hagfeldt, D. Bi, Perovskitoid-templated formation of a 1D@3D perovskite structure toward highly efficient and stable perovskite solar cells, Adv Energy Mater 11 (2021), https://doi.org/10.1002/aenm.202101018.
[45] M. Qin, H. Xue, H. Zhang, H. Hu, K. Liu, Y. Li, Z. Qin, J. Ma, H. Zhu, K. Yan, G. Fang, G. Li, U. Jeng, G. Brocks, S. Tao, X. Lu, Precise control of perovskite crystallization kinetics via sequential a-site doping, Adv. Mater. 32 (2020) 2004630, https://doi.org/10.1002/adma.202004630.
[46] C. Ge, J.-F. Lu, M. Singh, A. Ng, W. Yu, H. Lin, S. Satapathi, H. Hu, Mixed dimensional perovskites heterostructure for highly efficient and stable perovskite solar cells, Solar RRL 6 (2022) 2100879, https://doi.org/10.1002/solr.202100879.
[47] G. Liu, H. Zheng, J. Ye, S. Xu, L. Zhang, H. Xu, Z. Liang, X. Chen, X. Pan, Mixed-phase low-dimensional perovskite-assisted interfacial lead directional management for stable perovskite solar cells with efficiency over 24%, ACS Energy Lett 6 (2021) 4395–4404, https://doi.org/10.1021/acsenergylett.1c01878.
[48] T. Yang, C. Ma, W. Cai, S. Wang, Y. Wu, J. Feng, N. Wu, H. Li, W. Huang, Z. Ding, L. Gao, S. (Frank) Liu, K. Zhao, Amidino-based Dion-Jacobson 2D perovskite for efficient and stable 2D/3D heterostructure perovskite solar cells, Joule 7 (2023) 574–586, https://doi.org/10.1016/j.joule.2023.02.003.
[49] S.N. Habisreutinger, N.K. Noel, H.J. Snaith, R.J. Nicholas, Investigating the role of 4- *Tert* Butylpyridine in perovskite solar cells, Adv Energy Mater 7 (2017) 1601079, https://doi.org/10.1002/aenm.201601079.
[50] J. Qiu, Y. Zheng, Y. Xia, L. Chao, Y. Chen, W. Huang, Rapid crystallization for efficient 2D ruddlesden-popper (2DRP) perovskite solar cells, Adv Funct Mater 29 (2019) 1806831, https://doi.org/10.1002/adfm.201806831.